ACS OMEGA

Open Access

http://pubs.acs.org/journal/acsodf

Article

Stability of MoS_2 Nanocatalysts for the Slurry-Phase Catalytic Hydrogenation of Anthracene

Donge Wang, Chenggong Yang, Rong Huang, Hao Liu, Huaijun Ma, Wei Qu, and Zhijian Tian*

Cite This: *ACS Omega* 2024, 9, 23843−23852

Read Online

ACCESS | Metrics & More | Article Recommendations | Supporting Information

ABSTRACT: The stability of both the structure and activity of MoS_2 nanocatalysts is crucial for minimizing the catalyst cost of the slurry-phase (SP) catalytic hydrogenation. MoS_2-GP and MoS_2-SP catalysts were, respectively, obtained by gas-phase (denoted as GP) and SP aging of fresh MoS_2 catalysts. The MoS_2-SP catalyst demonstrated a comparable catalytic hydrogenation activity to that of the fresh MoS_2 catalyst, which is about 1.7 times of that for the MoS_2-GP catalyst. After 12 cycles of the MoS_2-SP catalyst, the obtained Cy12 catalyst demonstrates a retention of 92.0% of its initial catalytic activity. The MoS_2-SP catalyst exhibits an impressive stability of catalytic hydrogenation. The MoS_2-SP catalyst exhibits average stacking layers of 3.3 and an average slab of 5.2 nm and exposes 14.0% of active sites. The MoS_2-SP catalyst can serve as a highly active and stable catalyst for catalytic hydrogenation. This finding can offer valuable insights into the stability of the hydrogenation catalyst in SP hydrogenation technology.

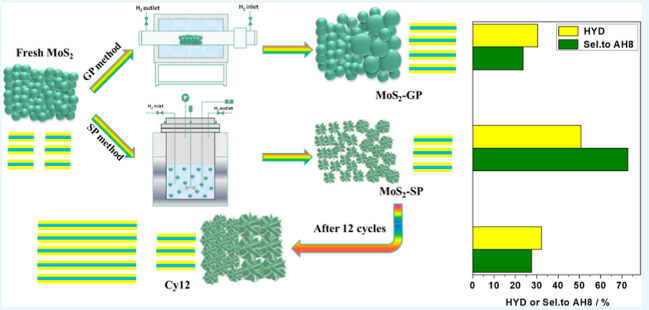

1. INTRODUCTION

The diminishing availability of light crude oil and the rising demand for clean, high-value fuels have encouraged petroleum refineries to upgrade low-value heavy feedstocks with a low H/C ratio, such as heavy oils, bitumen, and residual oils, into more valuable products like transportation light fuels.[1−3] The technologies applied in the refining industry to upgrade the heavy feedstocks involve thermal processes (carbon rejection) and catalytic processes (hydrogen addition).[4] However, the thermal processes give low yields of light oils by carbon rejection because these processes simultaneously generate lighter fractions and heavier fractions with respect to the feedstocks.[5] Moreover, the obtained light fractions often exhibit poor quality. The catalytic processes of heavy feedstocks can convert more efficiently heavy feedstocks into light fractions to enhance the H/C ratio of the products by hydrogen addition and thus prove to be more capable approaches to upgrade heavy feedstocks into light oils in comparison with the thermal processes.[6] Slurry-phase (SP) hydrogenation utilizing the dispersed catalyst can maximize the conversion of highly contaminated heavy feedstocks,[3,7−9] thus displaying the potential to efficiently upgrade heavy feedstocks. Therefore, it is essential to develop a highly active and stable catalyst to minimize the catalyst cost and improve the economy of SP hydrogenation technology.

The dispersed catalysts utilized in the reported SP hydrogenation technologies are predominantly focused on Fe- and Mo-based catalysts. The red mud containing hematite (Fe_2O_3) was utilized in upgrading vacuum residue with a batch SP reactor.[10] Natural limonites excavated from Brazilian and Australian mines were applied in the hydrocracking of Brazilian Marlim vacuum residue.[11] The Fe-based catalysts were synthesized through a process involving grinding, milling, sieving, and drying pieces of mineral ores such as magnetite, limonite, molybdenite, hematite, ferrite, and laterite.[12−14] The mineral ores were activated in situ by the sulfur released from the organosulfide compounds in heavy oils to form pyrrhotite ($Fe_{(x-1)}S_x$).[3] Using Fe-based natural ores and red mud as dispersed catalysts is attributed to their ready availability and low cost. Therefore, these Fe-based catalysts can be used once in the SP hydrogenation technology without recycling.

In the SP hydrogenation process, the highly active Mo-based catalysts are developed by constructing novel nanostructures and designing controllable synthesis routes.[15−17] However, MoS_2 catalysts are costly and usually utilized with the added Mo concentrations of above ∼300 ppm in the heavy feedstocks.[18] Hence, the catalyst recovery and reuse are pivotal to reduce the catalyst cost and improve the economy of the highly efficient SP hydrogenation technology of heavy feedstocks with Mo-based catalysts.[3,19] The remained dis-

Received: February 26, 2024
Revised: April 23, 2024
Accepted: April 29, 2024
Published: May 22, 2024

persed catalyst and the unconverted heavy oils are recycled to enhance the conversion of the feedstock, as shown by the ENI slurry technology during recycle processes.[20] Concerning the economy of Mo-based catalysts, the recycling of catalysts is imperative for the industrial application of SP hydrogenation of heavy oils. To preserve both catalytic activity and active structure, the SP processes necessitate Mo-based catalysts with high stability to reduce both the consumption and cost. Therefore, it is vital to undertake recycling and investigate the stability of the MoS_2 catalyst during the catalytic hydrogenation process.

The deactivation of the supported MoS_2 catalyst in other catalytic hydrogenation processes is generally caused by metal deposition, formation of coke, or physical effects, such as attrition or sintering.[21−24] However, exploring the stability of dispersed Mo-based hydrogenation catalysts has been undertaken infrequently in the past few decades. Rezaei et al. studied the stability of the MoS_2 catalyst by recovering the coke−catalyst mixture from the SP hydrogenation product of Cold Lake vacuum residue.[18,25] Findings from the recycling experiments revealed that the catalyst concentration and the changes in the chemical properties of the coke determined the deactivation rate of the catalyst during the hydrogenation process. Jeong et al. reported an in situ synthesized dispersed $MoWS_2$ catalyst for the hydrogenation of vacuum residue at 693 K and 9.5 MPa in H_2.[26] Transmission electron microscopy (TEM) analysis revealed that the morphology and average particle size of the $MoWS_2$ catalyst can be maintained for more than three cycles. Kim et al. investigated the structural properties of dispersed MoS_2 catalysts collected at different times for SP hydrogenation of vacuum residues.[27] Extended X-ray absorption fine structure and TEM analysis indicated that the dispersed MoS_2 catalyst deactivation can be attributed to the exposed and defect sites as active phases and the increase of slab size and stack as the process of SP hydrogenation of vacuum residue advanced. The spent MoS_2 hydrogenation catalysts in the reported works are often present in a mixture of catalysts with coke or unconverted residues. It poses challenges to effectively separate the spent hydrogenation catalysts from the coke or unconverted residues in the hydrogenation products. The problem of catalyst separation results from the peculiar physical and chemical properties of heavy feedstocks such as complex compositions, high viscosity, and more impurities. Therefore, it is almost impossible to research the inherent stability of hydrogenation catalysts in the SP hydrogenation of heavy feedstocks.

The asphaltenes are the heaviest component, high-molecular-weight, highly aromatic, and hydrogen-deficient solid substances in the heavy feedstocks.[28] The predominant asphaltene molecular architecture demonstrates the aromatic core of fused polycyclic aromatic hydrocarbon with various substituents such as naphthenic, short aliphatic side chains, and polar function groups.[29] Correspondingly, a polycyclic aromatic hydrocarbon, which is similar to the structure of the aromatic core in the asphaltenes, can be utilized as the model compound to investigate the catalytic hydrogenation activities of hydrogenation catalysts.[30,31] Fortunately, our previous results indicate that the MoS_2 hydrogenation catalysts exhibit similar trends of catalytic hydrogenation activities among the model compound anthracene, asphaltenes, and heavy feedstocks.[32] Therefore, anthracene can be utilized as the model compound of heavy feedstock to research the inherent stability of the MoS_2 hydrogenation catalyst.

Herein, the stability of the MoS_2 catalyst was explored by aging fresh MoS_2 catalyst with the gas-phase (GP) process and SP processes, and the obtained MoS_2 catalyst was reused for 12 cycles in the catalytic hydrogenation of anthracene to investigate its structure and activity stabilities. Compared with the fresh MoS_2 catalyst, the MoS_2 catalyst obtained by GP aging displayed a much lower activity of catalytic hydrogenation. The MoS_2 catalyst aged by an SP process exhibited comparable catalytic activity to that of the fresh MoS_2 catalyst. Furthermore, the catalytic activity of the MoS_2 catalyst obtained by SP aging after 12 cycles is about 92.0% of its initial catalytic activity. The characterization results indicate that the decrease of catalytic activity may result from the reduced exposure of active sites, which was caused by the enlargement of particle size and the slight increase of the stacking layers and slab with the increase of cycles.

2. EXPERIMENTAL SECTION

2.1. Materials. Elemental sulfur (S_8) and tridecane were purchased from the Aladdin Industrial Corporation. Ammonium heptamolybdate $[(NH_4)_6(Mo_7O_{24})\cdot 4H_2O]$, hydrazine monohydrate (80%), ethanol, and ethylene glycol ($HOCH_2CH_2OH$) were supplied by Tianjin Kermel Chemical Reagent Co. Ltd. Anthracene (AN) was obtained from J&K Scientific. Chemicals without special descriptions were purchased from commercial sources and used without further purification.

2.2. Synthesis of MoS_2 Nanocatalysts. Fresh MoS_2 nanocatalysts were synthesized by a solvothermal method referring to our previous work.[33] 2.1186 g of ammonium heptamolybdate $[(NH_4)_6(Mo_7O_{24})\cdot 4H_2O]$ and 1.1520 g of elemental sulfur were dissolved in 52 mL of ethylene glycol to form a suspension solution under constant stirring. Then, 8 mL of hydrazine monohydrate (80%) was added in the above solution. The solution was transferred to a Teflon-lined stainless-steel autoclave with the capacity of 100 mL. The autoclaves were heated in an electric oven to 180 °C, maintained for 48 h, and then cooled down naturally. A black product, the MoS_2 sample, was collected after being filtered, washed with distilled water and ethanol three times, and finally dried naturally. The obtained MoS_2 product was named fresh MoS_2.

Dispersed MoS_2 catalysts can be synthesized by aging fresh MoS_2 in H_2 through a GP process. 0.5 g of fresh MoS_2 catalyst was annealed at 350 °C for 3 h in a tube furnace under a H_2 atmosphere. The obtained MoS_2 catalyst was denoted as MoS_2-GP. Besides, dispersed MoS_2 catalysts can also be synthesized by aging fresh MoS_2 in the liquid system by an SP process. The detailed process is as follows. 1.0 g of fresh MoS_2 catalyst was treated in 30 mL of tridecane solvent containing 3.0 g of anthracene at 350 °C for 3 h with an initial H_2 pressure of 8 MPa in a Parr high-pressure autoclave. The MoS_2 sample was collected after being filtered with filter paper, washed with distilled water and ethanol three times, and finally dried in a vacuum oven at 70 °C for 12 h. The obtained MoS_2 catalyst was denoted as MoS_2-SP.

2.3. Characterizations of MoS_2 Catalysts. X-ray diffraction (XRD) patterns of MoS_2 catalysts were obtained using a PANalytical X′ Pert Pro X-ray diffractometer equipped a nickel-filtered Cu Kα radiation (λ = 0.15418 nm) with 40 kV and 40 mA. The scanning electron microscopy (SEM) and high resolution transmission electron microscopy (HRTEM) images of MoS_2 catalysts were, respectively, taken from a JSM-

https://doi.org/10.1021/acsomega.4c01846
ACS Omega 2024, 9, 23843−23852

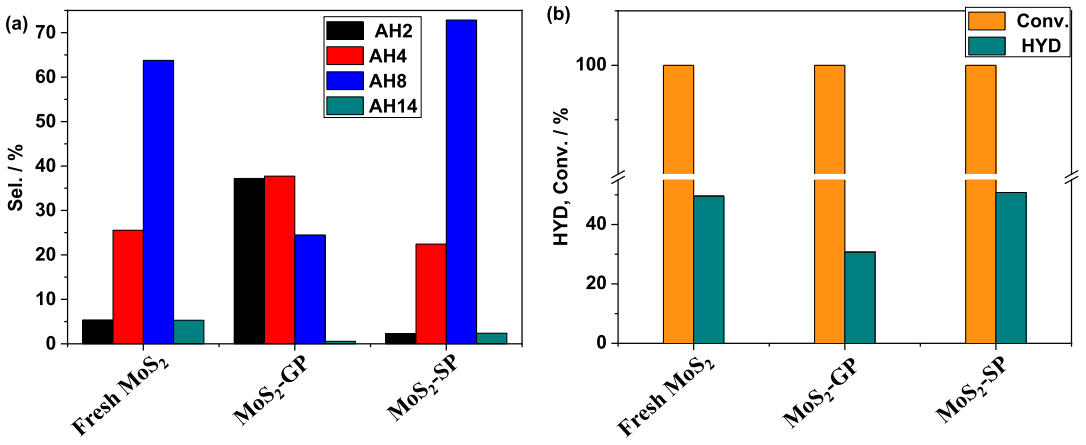

Figure 1. (a) Selectivity of AH*x* and (b) HYDs and conversions of AN hydrogenation with fresh MoS_2 and MoS_2 catalysts obtained by GP and SP aging. Catalyst, 0.075 g; AN, 3.0 g; solvent tridecane, 30.0 g; initial pressure, 8.0 MPa; reaction temperature, 350 °C; reaction time, 4 h.

7800F microscope and a JEM 2100F microscope. The surface areas of the MoS_2 catalysts were tested at 77 K with a Micromeritics ASAP 2420 analyzer. Raman spectra of MoS_2 catalysts were recorded on a Nano Wizard Renishaw Raman spectrometer, and a 532 nm single-frequency laser was used as the excitation source. Infrared spectra were obtained on a Thermo Scientific Nicolet iS-50 FTIR spectrometer equipped with a liquid nitrogen-cooled mercury−cadmium−telluride detector.

2.4. Catalytic Hydrogenation Performances of MoS_2 Catalysts. Catalytic activity for AN hydrogenation was evaluated with a Parr high-pressure microreactor of 100 mL. 30.0 g of tridecane solvent, 3.0 g of AN, and 0.075 g of MoS_2 catalysts were introduced into the microreactor. Hydrogen was purged into the microreactor three times to exchange the air in the reaction system, and subsequently the microreactor was charged with H_2 to the initial pressure of 8.0 MPa at room temperature. Hydrogenation reactions were conducted at 350 °C with a stirring rate of 300 rpm. The catalytic reaction was maintained for 4 h, and then the microreactor was allowed to naturally cool down. The liquid product was first extracted in a syringe from the reacted slurry and filtered with the syringe filter to ensure that the catalyst can remain in the reacted slurry. The syringe filter is made of organic nylon-66 with a pore size of 0.22 μm. Finally, the hydrogenation products were qualitatively and quantitatively analyzed with an Agilent 7890B/5977A gas chromatograph/mass spectrometer and an Agilent 7890A gas chromatograph, respectively. Both Agilent 7890A gas chromatograph and Agilent 7890B-5977A gas chromatograph-mass spectrometer were fitted with HP-5 columns and flame ionization detectors.

To assess the stability of the MoS_2 catalyst, the MoS_2-SP catalyst was separated from the reacted slurry after each hydrogenation reaction and once again added into the reactor to reuse for the next run of AN hydrogenation reaction. The detailed cycle experiment process is as follows. After each catalytic hydrogenation reaction, the liquid product was collected by filtering the catalyst with a syringe equipped with an organic syringe filter made of organic nylon-66 with a pore size of 0.22 μm. All the remaining reacted slurry in the reactor was transferred to the sample bottle, and the adhesive catalyst on the agitator arm, gas inlet pipe, and thermocouple tube was also collected by flushing them with tridecane into the sample bottle. The MoS_2 catalyst was separated by suction filtration of the obtained slurry with an organic filter membrane, which is also made of organic nylon-66 with a pore size of 0.22 μm. After being washed with tridecane and ethanol three times, the MoS_2 catalyst was dried in a vacuum oven. The obtained MoS_2 catalyst was used in the next run of catalytic hydrogenation reaction. The Cy12 catalyst was obtained after recycling the MoS_2-SP catalyst by catalytic hydrogenation 12 times.

The products of AN hydrogenation are mainly AN derivatives including 9,10-dihydroanthracene (denoted as AH2), tetrahydroanthracene (denoted as AH4), octahydroanthracene, and octahydrophenanthrene isomers (denoted as AH8), and several 2-perhydroanthracene isomers (denoted as AH14). The AN conversion, AN hydrogenation percentage, and product selectivity were calculated as follows.

The hydrogenation selectivity (denoted as Sel.) to AH*x* is as follows

$$\text{sel.}_{(\text{AH}x)}\ (\text{mol}\ \%) = \text{AT}_{(\text{AH}x)} \times 100 / [\text{AT}_{(\text{AH2})} + \text{AT}_{(\text{AH4})} + \text{AT}_{(\text{AH8})} + \text{AT}_{(\text{AH14})}] \quad (1)$$

$\text{AT}_{(\text{AH}x)}$ is the molar of AH*x*.

In the reaction system, no cracking products can be observed. Thus, this suggests that AN can retain the mass balance. The conversion (denoted as Conv.) is as follows

$$\text{conv.}\ (\%) = ([\text{AN}]_0 - [\text{AN}])/[\text{AN}]_0 \times 100\% \quad (2)$$

$[\text{AN}]_0$ means the initial concentration of AN and [AN] represents the final concentration of AN after catalytic hydrogenation reaction.

The degree of hydrogenation (denoted as HYD) of AN is calculated as follows

$$\text{HYD}\ (\%) = \text{conv.} \times [\text{sel.}_{(\text{AH2})} \times 2 + \text{sel.}_{(\text{AH4})} \times 4 + \text{sel.}_{(\text{AH8})} \times 8 + \text{sel.}_{(\text{AH14})} \times 14] \times 100/14 \quad (3)$$

$\text{Sel.}_{(\text{AH}x)}$ is the selectivity to the AN hydrogenation products and Conv. is the AN conversion. Hence, HYD represents the hydrogenation degree of AN, that is, the ratio between the real hydrogenation consumption in the AN hydrogenation reaction

https://doi.org/10.1021/acsomega.4c01846
ACS Omega 2024, 9, 23843−23852

and the theoretical hydrogenation consumption in the full hydrogenation saturation reaction "AN + 7H_2 to AH_{14}".

3. RESULTS AND DISCUSSION

Figure 1 displays the catalytic activities of AN hydrogenation with fresh MoS_2 and MoS_2 catalysts aged by GP and SP processes. Figure 1a illustrates the selectivities to the hydrogenation products (AHx) of AN hydrogenation over MoS_2 catalysts. The fresh MoS_2 catalyst exhibits a selectivity of 63.8% to the deep hydrogenation product AH8 of AN hydrogenation. The MoS_2-GP catalyst demonstrates a selectivity to AH8 of 24.5%, which is much lower than that over the fresh MoS_2 catalyst. The MoS_2-SP catalyst shows a selectivity of 72.9% to AH8, which is slightly higher than that over the fresh MoS_2 catalyst. Figure 1b shows that all the conversions of AN hydrogenation can exceed 99.0% with both the fresh MoS_2 catalyst and aged MoS_2 catalysts. HYD of 49.5% for AN hydrogenation can be achieved using the fresh MoS_2 catalyst. HYD of 30.7% over the MoS_2-GP catalyst for AN hydrogenation is much lower than that over the fresh MoS_2 catalyst. HYD of 50.8% over the MoS_2-SP catalyst is slightly higher than that over the fresh MoS_2 catalyst.

The GP aging of the fresh MoS_2 catalyst is unbeneficial to enhancing the catalytic activity of AN hydrogenation. However, the SP aging of the fresh MoS_2 catalyst can slightly improve the catalytic activity of AN hydrogenation. In general, the activities of AN hydrogenation are quite comparable with those of the MoS_2-SP catalyst and fresh MoS_2 catalyst.

Figure 2 displays the stability of the MoS_2-SP catalyst for 12 cycles of AN hydrogenation. During the recycling process, the

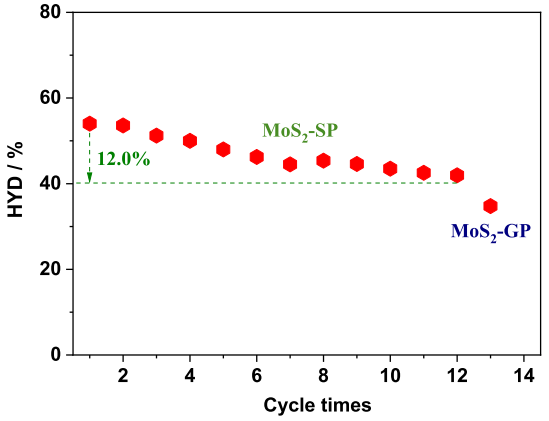

Figure 2. Stability of AN hydrogenation with the MoS_2-SP catalyst in the SP reactor. Catalyst, 0.15 g; AN, 3.0 g; solvent tridecane, 30.0 g; initial pressure, 8.0 MPa; reaction temperature, 350 °C; reaction time, 4 h.

HYD of AN gradually decreases with an increase in the recycle times of the MoS_2-SP catalyst. However, even after 12 cycles, the HYD of AN using the MoS_2-SP catalyst remains higher than that achieved in the initial use of the MoS_2-GP catalyst. After 12 cycles of the MoS_2-SP catalyst in Figure 2, the HYD of AN is decreased by 12.0%. That is, the HYD of AN in the 12th cycle remains at 77.7% of that in the first run. During the recycling process, the loss of the catalyst is inevitable. The recovery ratio of MoS_2-SP catalyst can reach 84.5% after 12 cycles of AN hydrogenation. The catalytic activity of the MoS_2-SP catalyst after 12 cycles has been reduced to 92.0% of the initial activity of the MoS_2-SP catalyst in the first run. Hence, the MoS_2-SP catalyst exhibits impressive stability of AN hydrogenation and can be effectively recycled in SP hydrogenation.

The catalytic hydrogenation activities of MoS_2 catalysts have no direct correlation with their BET surface areas of catalysts (Figure S1). Hence, it is necessary to explore the effect of structures on catalytic activity. In order to investigate the layer structures of MoS_2 catalysts, Figure 3 shows the Raman spectra

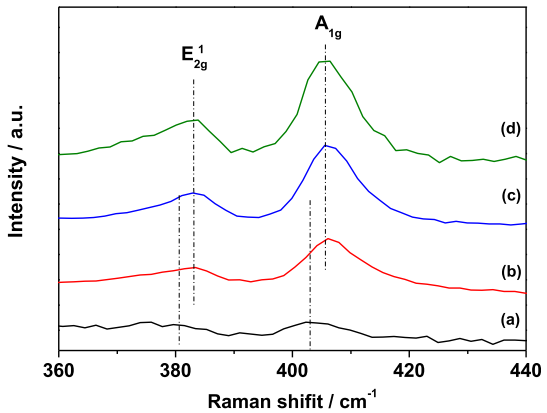

Figure 3. Raman spectra of (a) fresh MoS_2, (b) MoS_2-GP, (c) MoS_2-SP, and (d) Cy12 catalysts.

of fresh MoS_2 and MoS_2 catalysts obtained by GP and SP aging. Two characteristic Raman bands of 2H-MoS_2 at about 380 and 405 cm^{-1}, respectively, correspond to the in-plane Mo−S phonon mode (E_{2g}^1) and the out-of-plane Mo−S mode (A_{1g}) of a typical MoS_2 layered structure.[34] The shifts of Raman bands of MoS_2 catalysts are related with the in-plane Mo−S and the out-of-plane Mo−S vibrations, which may depend on the nanostructures of MoS_2 sheets.[35] No Raman bands corresponding to the J_1, J_2, and J_3 Mo−S phonon modes of 1T-MoS_2[36,37] can be observed from the Raman spectra of all the MoS_2 catalysts in Figure 3. Two poor Raman bands at ~381 and ~403 cm^{-1} from the Raman spectrum of the fresh MoS_2 catalyst in Figure 3a correspond to the in-plane and out-of-plane Mo−S modes of 2H-MoS_2. The Raman bands in Figure 3b−d for MoS_2-GP, MoS_2-SP, and Cy12 catalysts located at 383 and 405 cm^{-1} can also be ascribed to the Mo−S mode of 2H-MoS_2. No obvious shifts can be observed from the Raman spectra of MoS_2-GP, MoS_2-SP, and Cy12 catalysts, which implies that their layer structures are analogous. However, the Raman bands of MoS_2-GP, MoS_2-SP, and Cy12 catalysts slightly shift positively in comparison with those of the fresh MoS_2 catalyst. If the stacking layers of the MoS_2 catalyst increase, the interlayer van der Waals force of MoS_2 favors atom vibration, leading to higher force constants and blue shifts of Raman bands.[33,34,38] The blue shift of the Raman band for the MoS_2 catalyst may result from the increase of stacking layers. Besides, the stronger bands indicate fewer defects in the basal planes of MoS_2. The fewer defects in the basal plane can result in the higher order of MoS_2 nanosheets and lead to the larger particle size and better crystallinity for MoS_2 catalysts. Therefore, it can be concluded that MoS_2-GP, MoS_2-SP, and Cy12 catalysts may exhibit slightly larger particle size, better crystallinity, and more stacking layers than those of the fresh MoS_2 catalyst.

To further study the phase structure and layer structures, Figure 4 presents XRD patterns of fresh MoS_2 and MoS_2

https://doi.org/10.1021/acsomega.4c01846
ACS Omega 2024, 9, 23843−23852

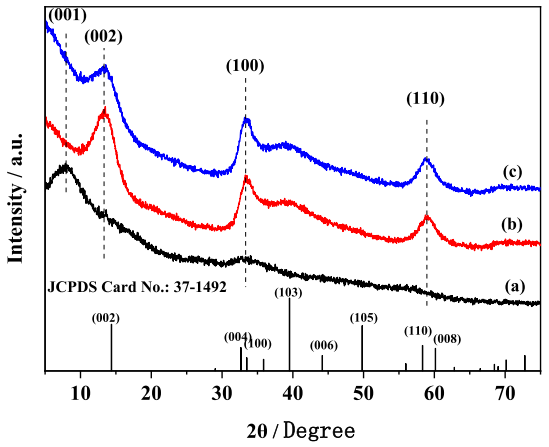

Figure 4. XRD patterns of (a) fresh MoS_2, (b) MoS_2-GP and (c) MoS_2-SP catalysts.

catalysts obtained by GP and SP aging. The broad and poor (001) diffraction peak located at 8.5° can be observed from the XRD pattern of the fresh MoS_2 catalyst in Figure 4a. According to our previous works,[32,33,39−42] the (001) peak results from the expansion of basal spacing induced by the intercalated species. According to Bragg's Law: $2d \sin\theta = n\lambda$, $n = 1, 2, ...$, the basal spacing d for fresh MoS_2 sample is about 1.04 nm. The typical (100) and (110) diffraction peaks at ∼32.7 and ∼57.2° correspond to hexagonal 2H-MoS_2 in the XRD pattern of the fresh MoS_2 catalyst in Figure 4a. The two diffraction peaks are broadened and very weak, which suggests a lower crystallinity of the fresh MoS_2 catalyst. Therefore, a fresh MoS_2 catalyst can be correspondingly assigned to the intercalated 2H-MoS_2 with lower crystallinity. From Figure 4b, the diffraction peaks at 13.6, 32.7, and 58.4° in the XRD patterns of MoS_2-GP catalysts can be correspondingly indexed to (002), (100), and (110) planes of hexagonal 2H-MoS_2 (JCPDS no. 37-1492). According to Bragg's law, the (002) diffraction peak at $2\theta = 13.6°$ in the XRD pattern of the MoS_2-GP catalyst corresponds to the basal spacing d of 0.65 nm in Table 1. In Figure 4c, the XRD pattern of the MoS_2-SP catalyst

Table 1. Calculated Layer Structures from the XRD Patterns of MoS_2 Catalysts[a]

catalysts	d/nm	D_{002}/nm	$\bar{n}$
fresh MoS_2	1.04		
MoS_2-GP	0.65	2.5	3.8
MoS_2-SP	0.65	2.1	3.2

[a]D_{002}: the thickness of MoS_2 nanosheets, $\bar{n}$: the average stacking layer number of MoS_2 nanosheets, d: the basal spacing of MoS_2 nanosheets.

can also be assigned to hexagonal 2H-MoS_2. The MoS_2-SP catalyst possesses the basal spacing of 0.65 nm, which is the same as that of the ,MoS_2-GP catalyst. After aging by GP and SP processes, the intercalated species in the fresh MoS_2 catalyst escaped from the interlayers, and the (002) diffraction peak can be observed in the XRD patterns of MoS_2-GP and MoS_2-SP catalysts.

The (002) peak originates from the interference of MoS_2 layers along the c-axis and represents the periodic sequence of MoS_2 layers in the c-axis.[43−45] Therefore, according to the Debye−Scherrer equation, the thickness of MoS_2 nanosheets along the c axis in MoS_2 catalysts can be calculated with the full width at half-maximum (fwhm) of the (002) peak. The fwhm's of the (002) peaks were measured directly from the X-ray patterns to determine crystallite dimensions of the MoS_2 slabs in the c-axis direction using the Debye−Scherrer relation: $D_{002} = \frac{K_{002}\lambda}{\beta_{002}\cos\theta}$, where D_{002} is the dimension of MoS_2 particle along the c direction, that is, the thickness of MoS_2 nanosheets. λ is the wavelength of the X-rays, and θ is the diffraction angle and β_{002} (or fwhm) is the angular line width. k_{002} is the shape factor of MoS_2. It is noteworthy that the determination of the stacking degree using the Debye−Scherrer equation for the (002) peak can give an average height for the stacked layers. The apparent average stacking layer number $\bar{n}$ can be calculated through dividing MoS_2 thickness by basal spacing with the following equation: $\bar{n} = D_{002}/d$, where d corresponds to the basal spacing in the 2H-MoS_2 nanosheets. The obtained thicknesses D_{002} and average layer numbers $\bar{n}$ of MoS_2 nanosheets are summarized in Table 1. The calculated stacking layer number is 3.8 for the MoS_2-GP catalyst. The calculated stacking layer number is 3.2 for the MoS_2-SP catalyst. The MoS_2-GP catalyst exhibits more stacking layers compared to the MoS_2-SP catalyst.

To visually inspect the layer structures of MoS_2 catalysts, Figure 5 displays the HRTEM images of fresh MoS_2, MoS_2-GP, MoS_2-SP, and Cy12 catalysts. From the HRTEM images of the fresh MoS_2 catalyst in Figure 5a,b, the stacking layer number is less than 4, and the slab length is 3−7 nm. For the MoS_2-GP catalyst, the stacking layer number of partial MoS_2 nanosheets exceeds 4, reaching as high as 7, and the slab length

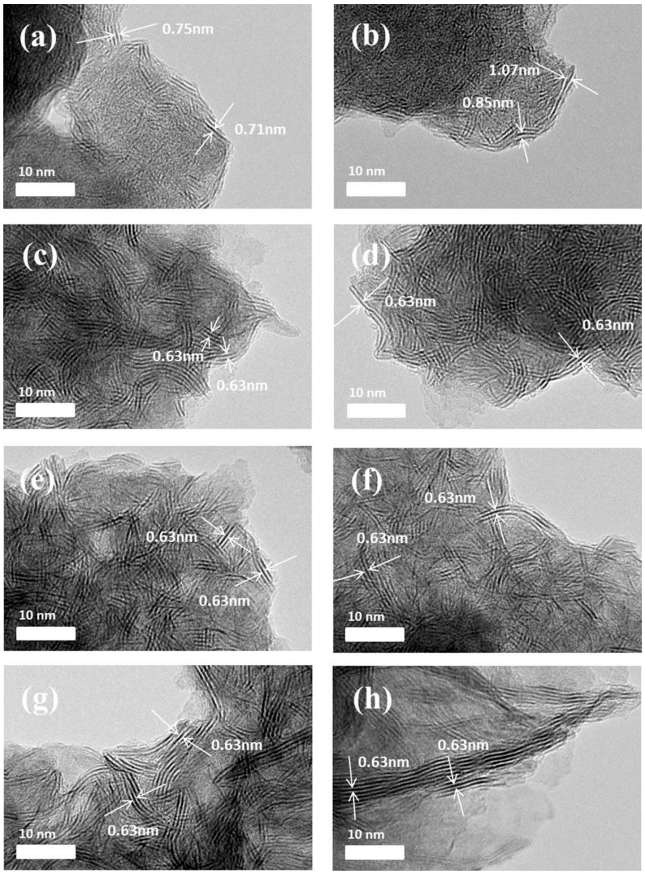

Figure 5. HRTEM images of (a,b) fresh MoS_2, (c,d) MoS_2-GP, (e,f) MoS_2-SP, and (g,h) Cy12 catalysts.

https://doi.org/10.1021/acsomega.4c01846
ACS Omega 2024, 9, 23843−23852

can extend beyond 10 nm in Figure 5c,d. From Figure 5e,f, the stacking layer number of MoS_2-SP catalyst remains less than 4, which is comparable to that of fresh MoS_2 catalysts, but the slab length of partial MoS_2-SP nanosheets increase to approximately 10 nm. From the HRTEM images in Figure 5g,h, two layer structures can be observed in the Cy12 catalyst. As shown in Figure 5g, the majority of MoS_2 nanosheets in the Cy12 catalyst display the stacking layers of less than 5 and slab of 5−15 nm. A minority of MoS_2 nanosheets in Figure 5h exhibit stacking layers of more than 5 and slab lengths exceeding 30 nm. The TEM images in Figure S2g,h confirm that the Cy12 catalyst contains nanoparticles with particle sizes both smaller than 100 nm and larger than 200 nm. With increasing recycle times of the MoS_2-SP catalyst, its stacking layers, slab length, and particle size increase gradually.

Based on the HRTEM images in Figure 5, in order to accurately describe the layer structures, the average stacking layer numbers and average slab lengths of MoS_2 nanosheets in MoS_2 catalysts are summarized in Table 2 through collecting

Table 2. Layer Structures of MoS_2 Catalysts Obtained by the Statistical Results of the HRTEM Images

layer structures of MoS_2 catalysts	average stacking layer numbers ($\bar{N}$)	average slab length ($\bar{L}$)/nm	R_{Mo}/at. %
fresh MoS_2	3.0	3.1	24.6
MoS_2-GP	3.9	5.8	10.7
MoS_2-SP	3.3	5.2	14.0
Cy12	3.6	5.2	12.8

statistical results of more than 100 nanosheets for each MoS_2 catalyst in Figure S3. The average stacking layer number and slab length of the fresh MoS_2 catalyst are 3.0 and 3.1 nm, respectively. For the MoS_2-GP catalyst, the average stacking layer and slab length are, respectively, increased to 3.9 and 5.8 nm. For the MoS_2-SP catalyst, the average stacking layer and slab length exhibit a slight increase to 3.3 and 5.2 nm, respectively. For MoS_2-GS and MoS_2-SP catalysts, the average stacking layers derived from the statistical results of HRTEM images are very consistent with those calculated using the Bragg equation and Debye−Scherrer equation. Table 2 only gives the layer structures of partial Cy12 catalyst with the particle size smaller than 100 nm, which exhibits average stacking layers of 3.6 and slab length of 5.2 nm. The Cy12 catalyst with a particle size of larger than 100 nm possesses more stacking layers and larger slabs. Due to the aggregation of large MoS_2 nanosheets, it is difficult to collect statistical data of the layer structure of large aggregated Cy12 particles.

The average lateral sizes of MoS_2 nanosheets $\bar{L}$ and the average stacking layer numbers of MoS_2 nanosheets $\bar{N}$ obtained from micrographs were processed by a statistical analysis and calculated according to eqs 4 and 5 with the weighted arithmetic mean method.[46,47] Mo dispersion in all of the edges of S−Mo−S layers can be defined by the ratio of Mo at the edge planes and in all of the MoS_2 catalysts. Based on the assumption that sulfide plates are perfect hexagons,[48] it is estimated that Mo dispersion (D_{Mo}) can be obtained by dividing the total number of Mo atoms on the edge planes (Mo_{edge}) by the total number of Mo atoms (Mo_{total}) in the whole MoS_2 nanosheets according to eq 6 using the lateral sizes measured in the TEM images.[47−49] According to eq 6, D_{Mo} is correlated with the average lateral size and is independent of the average stacking layer number.

As reported by our previous work,[34] the active sites of catalytic hydrogenation on MoS_2 catalysts are located at the edges of upper and bottom S−Mo−S layers, which are named as Rim site by Daage and Chianelli.[50] The exposure percentages of Rim site Mo (denoted as R_{Mo}) can be calculated according the eq 7.[42,47,51] So R_{Mo} is dependent on both the average lateral size and average stacking layer number. In order to quantitatively express the exposure of active sites for catalytic hydrogenation, R_{Mo} for MoS_2 sheets can be deduced according to eq 7 when $\bar{N}$ is larger than 2. If $\bar{N}$ is equal to or less than 2, R_{Mo} is equal to D_{Mo}. The value of R_{Mo} is 24.6% for the fresh MoS_2 catalyst as shown in Table 2. In contrast, R_{Mo} is only 10.7% for the MoS_2-GP catalyst. 14.0% of R_{Mo} for the MoS_2-SP catalyst is higher than that for the MoS_2-GP catalyst. It can be concluded that the MoS_2-SP catalyst can expose more active sites than the MoS_2-GP catalyst. For the partial Cy12 catalyst with a smaller particle size, the value of R_{Mo} is slightly reduced to 12.8%. The other bulk aggregated Cy12 particles should have much lower exposure of Rim sites Mo due to their more stacking layers and longer slab.

The average lateral size $\bar{L}$ of the MoS_2 slab was calculated as follows

$$\bar{L} = \frac{\sum_{i=1\cdots x} x_i l_i}{\sum_{i=1\cdots x} x_i} \tag{4}$$

The average stacking layer number $\bar{N}$ of the MoS_2 slab was calculated as follows

$$\bar{N} = \frac{\sum_{i=1\cdots n} x_i \cdot N_i}{\sum_{i=1\cdots n} x_i} \tag{5}$$

MoS_2 dispersion (D_{Mo}) was calculated with the following equation

$$D_{Mo} = \frac{Mo_{edge}}{Mo_{total}} = \frac{\sum_{i=1\cdots n} 6n_i - 6}{\sum_{i=1\cdots n} 3n_i^2 - 3n_i + 1} \tag{6}$$

The exposure percentages of Rim sites Mo (R_{Mo}) can be calculated as follows

$$R_{Mo} = D_{Mo} \times \frac{2}{\bar{N}} \times 100\% = \frac{\sum_{i=1\cdots n} 6n_i - 6}{\sum_{i=1\cdots n} 3n_i^2 - 3n_i + 1} \times \frac{2}{\bar{N}} \times 100\% \tag{7}$$

In eq 4−7, L_i: length of slab; x_i: number of layers with length of L_i; N_i: number of stacks; $L = 3.2(2n_i - 1)$ Å; n_i: the number of Mo atoms on the edge of MoS_2.

It should be noted that the fresh MoS_2 catalyst has much higher exposure of Rim site Mo than that of the MoS_2-SP catalyst in Table 2, but exhibits comparative catalytic hydrogenation activity versus that of the MoS_2-SP catalyst. The fresh MoS_2 catalyst was synthesized with ethylene glycol as the solvent. Ethylene glycol with high viscosity may remain on the surface of fresh MoS_2 catalyst and thus may cover partial active sites of catalytic hydrogenation. It is known that the residual ethylene glycol in the catalyst can be detected by the infrared spectra.[52,53] The infrared spectra of fresh MoS_2, MoS_2-GP, and MoS_2-SP catalysts are given in Figure 6. In the IR spectrum of the fresh MoS_2 catalyst, three bands at 1630, 1420 and 1120 cm^{-1} can be correspondingly ascribed to the bending vibration of the OH group, the deformation vibration of the C−H group, and the stretching vibration of the C−O

https://doi.org/10.1021/acsomega.4c01846
ACS Omega 2024, 9, 23843−23852

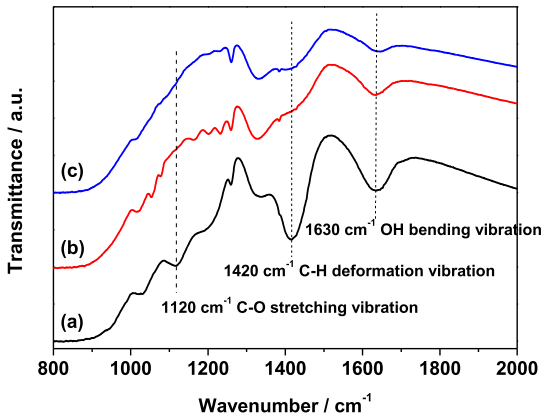

Figure 6. Infrared spectra of (a) fresh MoS_2, (b) MoS_2-GP, and (c) MoS_2-SP catalysts.

group. The OH, C−H, and C−O groups may result from the residual ethylene glycol on the surface of fresh MoS_2 catalyst. However, these bands cannot be observed from the infrared spectra of MoS_2-GP and MoS_2-SP catalysts. The results of IR spectra indicate that ethylene glycol can only be observed in fresh MoS_2 catalyst and can be totally removed after aging during both GP and SP processes. Therefore, the partial Rim site Mo in the fresh MoS_2 catalyst may be covered by the residual ethylene glycol; thus, actually, the accessible active sites in the fresh MoS_2 catalyst are lower than the calculated percentage of active sites in Table 2. No Rim sites Mo are covered in MoS_2-GP and MoS_2-SP catalysts; hence, all the Rim sites Mo can serve as the active sites for the catalytic hydrogenation of AN. Consequently, the fresh MoS_2 catalyst exhibits a lower activity than anticipated and displays a comparable activity to the MoS_2-SP catalyst.

Beyond the layer structures of MoS_2 catalysts, the morphologies and particle sizes were further investigated to explore the structure−activity relationship of MoS_2 catalysts. Figure 7 displays SEM images of MoS_2 catalysts with various magnifications. Figure 7a−c exhibits that the fresh MoS_2 catalyst consists of aggregated nanoparticles with particle sizes smaller than 50 nm. The MoS_2-GP catalyst demonstrates both nanoparticles smaller than 50 nm and aggregates larger than 100 nm in Figures 7d−f. From the SEM images in Figures 7g−i, the MoS_2-SP catalyst displays flower-like particles with particle sizes of smaller than 50 nm and about 100 nm assembled by MoS_2 nanosheets. After 12 cycles of the catalytic hydrogenation reactions with the MoS_2-SP catalyst, the partial particles of the obtained Cy12 catalyst still possess particle sizes of smaller than 100 nm; meanwhile, bulk aggregates assembled by MoS_2 nanosheets can be observed, with particle

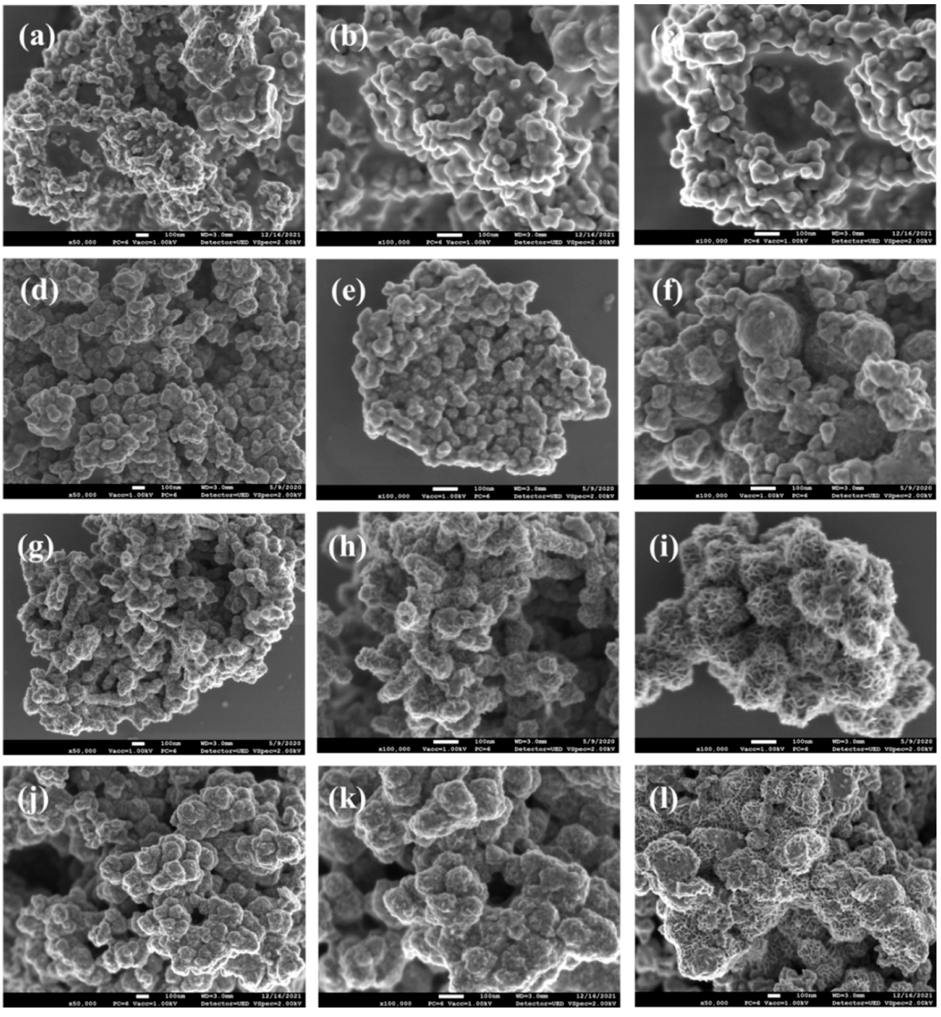

Figure 7. SEM images of (a−c) fresh MoS_2, (d−f) MoS_2-GP, (g−i) MoS_2-SP, and (j−l) Cy12 catalysts.

https://doi.org/10.1021/acsomega.4c01846
ACS Omega 2024, 9, 23843−23852

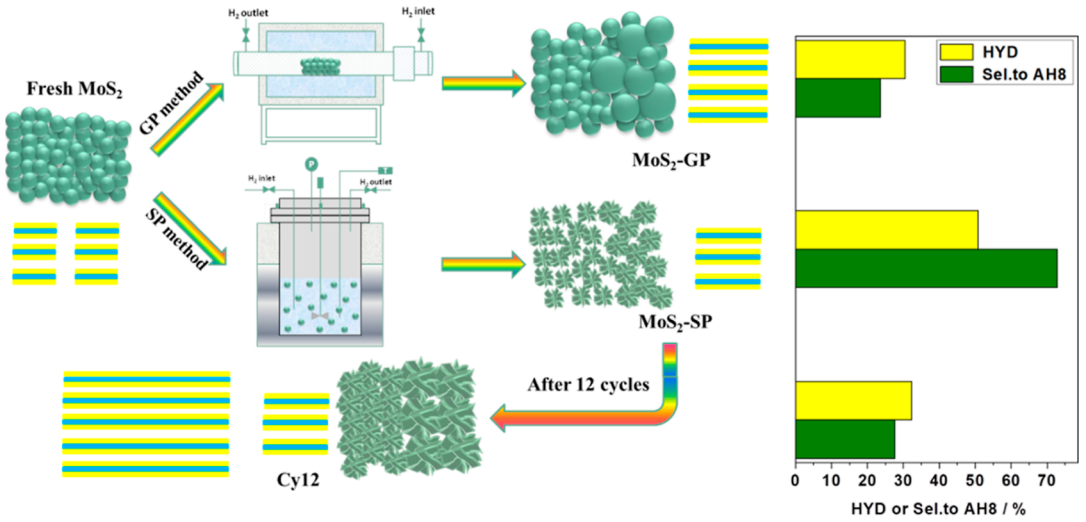

Figure 8. Schematic diagram of structure and performance of MoS_2 catalysts in the catalytic hydrogenation of anthracene. HYD: hydrogenation degree, Sel.: selectivity, AH8: octahydroanthracene and octahydrophenanthrene isomers.

sizes exceeding 100 nm. It can be speculated that the MoS_2-SP catalyst gradually grows into large particles with the increase of cycles, but the nanosheet morphology can be retained in the obtained Cy12 catalyst.

The structure-activity relationship is illustrated in Figure 8. The fresh MoS_2 catalyst synthesized at 180 °C using a solvothermal method possesses the smallest particle size of about 50 nm, fewest stacking layers, and shortest slab, thus exposing 24.6% of Rim sites Mo as the active sites. The fresh MoS_2 catalyst was aged in a tube furnace by a GP process under a H_2 atmosphere at 350 °C for 3 h to generate the MoS_2-GP catalyst. In comparison with the fresh MoS_2 catalyst, the obtained MoS_2-GP catalyst exhibits aggregated particles with size of larger than 100 nm, the most stacking layers, and longest slab, and it exposes 10.7% of Rim sites Mo, which is significantly lower than that of the fresh MoS_2 catalyst. The aggregated particles may be generated by the sintering of fresh MoS_2 nanoparticles during the GP aging process. The MoS_2-GP catalyst exhibits a much lower catalytic activity of AN hydrogenation with a HYD of 30.4% than that of the fresh MoS_2 catalyst with a HYD of 49.5%. The fresh MoS_2 catalyst was aged in an autoclave by an SP aging process under a H_2 atmosphere at 350 °C for 3 h to generate the MoS_2-SP catalyst. The generated MoS_2-SP catalyst demonstrates loose flower-like particles assembled by MoS_2 nanosheets and possesses approximate stacking layers and a slightly longer slab compared with the fresh MoS_2 catalyst. The MoS_2-SP catalyst exposes 14.0% of Rim sites Mo, which is higher than that of the MoS_2-GP catalyst but considerably lower than that of the fresh MoS_2 catalyst. Although the fresh MoS_2 catalyst exposes the most active sites, partial active sites are covered by the residual ethylene glycol on the surface of the fresh MoS_2 catalyst. Therefore, in comparison with the fresh MoS_2 catalyst, the MoS_2-SP catalyst exhibits a comparable catalytic activity of AN hydrogenation with HYD of 50.8%, which is much higher than that of 30.4% for the MoS_2-GP catalyst. The MoS_2-SP catalyst was recycled after 12 cycles of AN hydrogenation and named as the Cy12 catalyst. The partial Cy12 catalyst exhibits nanoparticles with a size smaller than 100 nm, average stacking layer number of 3.6, slab length of 5.2 nm, and exposes 12.8% of Rim sites Mo. The other Cy12 catalyst displays bulk aggregated particles assembled by MoS_2 nanosheets and possesses a particle size larger than 200 nm, stacking layer of more than 5, and a slab of longer than 30 nm. Nevertheless, the Cy12 catalyst still demonstrates a slightly higher HYD of 32.3% for AN hydrogenation than that of the MoS_2-GP catalyst. Therefore, the SP process is much more efficient than the GP process for the aging of the fresh MoS_2 catalyst.

4. CONCLUSIONS

The aging process can influence the stability of both activity and nanostructures in the MoS_2 catalyst during the catalytic hydrogenation reaction. Compared with the GP aging, the SP aging can enable the MoS_2-SP catalyst to exhibit a higher catalytic activity and better stability than the MoS_2-GP catalyst. The MoS_2-SP catalyst displays a catalytic activity comparable to that of the fresh MoS_2 catalyst. The Cy12 catalyst obtained after 12 cycles of the MoS_2-SP catalyst in the catalytic hydrogenation reaction can achieve 92.0% of the initial catalytic activity in the first cycle of the MoS_2-SP catalyst. According to the characterization results, the MoS_2-SP catalyst exposes more active sites for catalytic hydrogenation, which results from its few stacking layers, short slab, and small particle size. As the recycling advances, the MoS_2-SP catalyst gradually aggregates and grows into larger particles with more stacking layers and a longer slab. After 12 cycles, the Cy12 catalyst exposes slightly fewer active sites than those of the MoS_2-SP catalyst, which accounts for the decrease of catalytic activity during the 12 cycles. The MoS_2-SP catalyst can serve as the highly active and stable catalyst for the catalytic hydrogenation reaction. Studying the stability of hydrogenation catalysts can enhance our theoretical understanding of the reduction in catalyst costs during the upgrading of heavy oils into light oils using SP hydrogenation technology.

■ ASSOCIATED CONTENT

Supporting Information

The Supporting Information is available free of charge at https://pubs.acs.org/doi/10.1021/acsomega.4c01846.

BET surface areas, TEM images, and distributions of stacking layer numbers and slab lengths of fresh MoS_2, MoS_2-GP, MoS_2-SP, and Cy12 catalysts (PDF)

https://doi.org/10.1021/acsomega.4c01846
ACS Omega 2024, 9, 23843−23852

AUTHOR INFORMATION

Corresponding Author

Zhijian Tian − *Dalian National Laboratory for Clean Energy, Dalian Institute of Chemical Physics, Chinese Academy of Sciences, Dalian 116023, China; State Key Laboratory of Catalysis, Dalian Institute of Chemical Physics, Chinese Academy of Sciences, Dalian 116023, China;* orcid.org/0000-0002-6092-485X; Email: tianz@dicp.ac.cn

Authors

Donge Wang − *Dalian National Laboratory for Clean Energy, Dalian Institute of Chemical Physics, Chinese Academy of Sciences, Dalian 116023, China*

Chenggong Yang − *Dalian National Laboratory for Clean Energy, Dalian Institute of Chemical Physics, Chinese Academy of Sciences, Dalian 116023, China; University of Chinese Academy of Sciences, Beijing 100049, China;* orcid.org/0000-0001-9598-9699

Rong Huang − *Dalian National Laboratory for Clean Energy, Dalian Institute of Chemical Physics, Chinese Academy of Sciences, Dalian 116023, China; University of Chinese Academy of Sciences, Beijing 100049, China*

Hao Liu − *Dalian National Laboratory for Clean Energy, Dalian Institute of Chemical Physics, Chinese Academy of Sciences, Dalian 116023, China*

Huaijun Ma − *Dalian National Laboratory for Clean Energy, Dalian Institute of Chemical Physics, Chinese Academy of Sciences, Dalian 116023, China*

Wei Qu − *Dalian National Laboratory for Clean Energy, Dalian Institute of Chemical Physics, Chinese Academy of Sciences, Dalian 116023, China*

Complete contact information is available at: https://pubs.acs.org/10.1021/acsomega.4c01846

Author Contributions

The manuscript was written through contributions of all authors. All authors have given approval to the final version of the manuscript.

Notes

The authors declare no competing financial interest.

ACKNOWLEDGMENTS

This work was supported by the National Natural Science Foundation of China (grant no. 22272168) and Dalian Institute of Chemical Physics (grant no. DICP I202235).

ABBREVIATIONS

GP, gas phase; SP, slurry phase; AN, anthracene; AH2, 9,10-dihydroanthracene; AH4, tetrahydroanthracene; AH8, octahydroanthracene and octahydrophenanthrene isomers; AH14, perhydroanthracene isomers; HYD, hydrogenation degree

REFERENCES

(1) U.S. Energy Information Administration. *Annual Energy Outlook 2018 with Projections to 2050*; U.S. Department of Energy: Washington, DC, 2018.

(2) Prajapati, R.; Kohli, K.; Maity, S. K.; Garg, M. O. Coking Propensity During Hydroprocessing of Vacuum Residues, Deasphalted Oils, and Asphaltenes. *Fuel* **2017**, *203*, 514−521.

(3) Al-Attas, T. A.; Ali, S. A.; Zahir, M. H.; Xiong, Q.; Al-Bogami, S. A.; Malaibari, Z. O.; Razzak, S. A.; Hossain, M. M. Recent Advances in Heavy Oil Upgrading Using Dispersed Catalysts. *Energy Fuels* **2019**, *33*, 7917−7949.

(4) Taborda, E. A.; Franco, C. A.; Ruiz, M. A.; Alvarado, V.; Cortes, F. B. Experimental and Theoretical Study of Viscosity Reduction in Heavy Crude Oils by Addition of Nanoparticles. *Energy Fuels* **2017**, *31*, 1329−1338.

(5) Bellussi, G.; Rispoli, G.; Molinari, D.; Landoni, A.; Pollesel, P.; Panariti, N.; Millini, R.; Montanari, E. The Role of MoS_2 Nano-Slabs in the Protection of Solid Cracking Catalysts for the Total Conversion of Heavy Oils to Good Quality Distillates. *Catal. Sci. Technol.* **2013**, *3*, 176−182.

(6) Bellussi, G.; Rispoli, G.; Landoni, A.; Millini, R.; Molinari, D.; Montanari, E.; Moscotti, D.; Pollesel, P. Hydroconversion of Heavy Residues in Slurry Reactors: Developments and Perspectives. *J. Catal.* **2013**, *308*, 189−200.

(7) Nguyen, M. T.; Nguyen, N. T.; Cho, J.; Park, C.; Park, S.; Jung, J.; Lee, C. W. A Review on the Oil-Soluble Dispersed Catalyst for Slurry-Phase Hydrocracking of Heavy Oil. *J. Ind. Eng. Chem.* **2016**, *43*, 1−12.

(8) Kang, K. H.; Kim, G. T.; Park, S.; Seo, P. W.; Seo, H.; Lee, C. W. A Review on the Mo-Precursors for Catalytic Hydroconversion of Heavy Oil. *J. Ind. Eng. Chem.* **2019**, *76*, 1−16.

(9) Prajapati, R.; Kohli, K.; Maity, S. K. Slurry Phase Hydrocracking of Heavy Oil and Residue to Produce Lighter Fuels: An Experimental Review. *Fuel* **2021**, *288*, 119686.

(10) Nguyen-Huy, C.; Kweon, H.; Kim, H.; Kim, D. K.; Kim, D. W.; Oh, S. H.; Shin, E. W. Slurry-Phase Hydrocracking of Vacuum Residue with a Disposable Red Mud Catalyst. *Appl. Catal., A* **2012**, *447*−*448*, 186−192.

(11) Matsumura, A.; Kondo, T.; Sato, S.; Saito, I.; de Souza, W. F. Hydrocracking Brazilian Marlim vacuum residue with natural limonite. Part 1: catalytic activity of natural limonite. *Fuel* **2005**, *84*, 411−416.

(12) Quitian, A.; Ancheyta, J. Experimental Methods for Developing Kinetic Models for Hydrocracking Reactions with Slurry-Phase Catalyst Using Batch Reactors. *Energy Fuels* **2016**, *30*, 4419−4437.

(13) Sharypov, V. I.; Kuznetsov, B. N.; Beregovtsova, N. G.; Reshetnikov, O. L.; Baryshnikov, S. V. Modification of Iron Ore Catalysts for Lignite Hydrogenation and Hydrocracking of Coal-Derived Liquids. *Fuel* **1996**, *75*, 39−42.

(14) Sollberger, F. G.; Do, P.; Bhattacharyya, A.; Baird, L. A. Process for Slurry Hydrocracking Using Catalyst with Low Diaspore Alumina. U.S. Patent 10,703,990 B2, 2020.

(15) Prajapati, R.; Kohli, K.; Maity, S. K.; Sharma, B. K. Ultrafine Reverse Micelle Catalysts for Slurry-Phase Residue Hydrocracking. *Catal. Today* **2020**, *358*, 228−236.

(16) Prajapati, R.; Kohli, K.; Maity, S. K. Role of Catalyst Defect Sites Towards Product Selectivity in the Upgrading of Vacuum Residue. *Fuel* **2022**, *314*, 123062.

(17) Khadzhiev, S. N. Nanoheterogeneous catalysis: Definition, state, and research prospects (Review). *Pet. Chem.* **2016**, *56*, 465−479.

(18) Rezaei, H.; Ardakani, S. J.; Smith, K. J. Study of MoS_2 Catalyst Recycle in Slurry-Phase Residue Hydroconversion. *Energy Fuels* **2012**, *26*, 6540−6550.

(19) Furimsky, E. *Catalysts for Upgrading Heavy Petroleum Feeds*; Elsevier: Amsterdam, 2007; Vol. *169*.

(20) Browning, B.; Alvarez, P.; Jansen, T.; Lacroix, M.; Geantet, C.; Tayakout-Fayolle, M. A Review of Thermal Cracking, Hydrocracking, and Slurry Phase Hydroconversion Kinetic Parameters in Lumped Models for Upgrading Heavy Oils. *Energy Fuels* **2021**, *35*, 15360−15380.

(21) Maity, S. K.; Perez, V. H.; Ancheyta, J.; Rana, M. S.; Centeno, G. Effect of Asphaltene Contained in Feed on Deactivation of Maya Crude Hydrotreating Catalyst. *Pet. Sci. Technol.* **2007**, *25*, 241−249.

(22) Millan, M.; Adell, C.; Hinojosa, C.; Herod, A. A.; Dugwell, D.; Kandiyoti, R. Effect of Catalyst Deactivation and Reaction Time on Hydrocracking Heavy Hydrocarbon Liquids. *Energy Fuels* **2007**, *21*, 1370−1378.

(23) Stratiev, D. S.; Shishkova, I. K.; Nikolaychuk, E.; Anastasov, M.; Stanulov, K.; Toteva, V. Effect of Catalyst Condition on

Sedimentation and Conversion in the Ebullated Bed Vacuum Residue H-Oil Hydrocracking. *Pet. Sci. Technol.* **2019**, *37*, 1463−1470.
(24) Angeles, M. J.; Leyva, C.; Ancheyta, J.; Ramirez, S. A Review of Experimental Procedures for Heavy Oil Hydrocracking with Dispersed Catalyst. *Catal. Today* **2014**, *220*−*222*, 274−294.
(25) Rezaei, H.; Smith, K. J. Catalyst Deactivation in Slurry-Phase Residue Hydroconversion. *Energy Fuels* **2013**, *27*, 6087−6097.
(26) Jeong, H. R.; Kim, K. D.; Lee, Y. K. Highly Active and Stable $MoWS_2$ Catalysts in Slurry Phase Hydrocracking of Vacuum Residue. *J. Catal.* **2020**, *390*, 117−125.
(27) Kim, S. H.; Kim, K. D.; Lee, Y. K. Effects of Dispersed MoS_2 Catalysts and Reaction Conditions on Slurry Phase Hydrocracking of Vacuum Residue. *J. Catal.* **2017**, *347*, 127−137.
(28) Wang, X.; Ma, H.; Wang, D.; Wang, L.; Yang, Y.; Han, J.; Qu, W.; Yang, L.; Wang, S.; Tian, Z. Slurry-Phase Hydrogenation of Different Asphaltenes to Liquid Fuels on Dispersed MoS_2 Nanocatalysts. *ACS Omega* **2023**, *8*, 16384−16394.
(29) Groenzin, H.; Mullins, O. C. Asphaltene Molecular Size and Structure. *J. Phys. Chem. A* **1999**, *103*, 11237−11245.
(30) Muldakhmetov, Z. M.; Ordabaeva, A. T.; Meiramov, M. G.; Gazaliev, A. M.; Kim, S. V. Catalytic Hydrogenation of Anthracene on Binary (Bimetallic) Composite Catalysts. *Catalysts* **2023**, *13*, 957.
(31) Ordabaeva, A. T.; Muldakhmetov, Z. M.; Gazaliev, A. M.; Meiramov, M. G.; Zhivotova, T. S. Hydrocatalytic Treatment of a Broad Coal Tar Fraction. *Coke Chem.* **2023**, *66*, 220−226.
(32) Zheng, A.; Wang, D.; Wang, L.; Han, J.; Ma, H.; Pan, Z.; Qu, W.; Wang, C.; Tian, Z. Highly Efficient MoS_2 Nanocatalysts for Slurry-Phase Hydrogenation of Unconventional Feedstocks into Fuels. *Energy Fuels* **2021**, *35*, 2590−2601.
(33) Jiang, Y.; Wang, D.; Li, J.; Li, M.; Pan, Z.; Ma, H.; Lv, G.; Qu, W.; Wang, L.; Tian, Z. Designing MoS_2 Nanocatalysts with Increased Exposure of Active Edge Sites for Anthracene Hydrogenation Reaction. *Catal. Sci. Technol.* **2017**, *7*, 2998−3007.
(34) Li, H.; Zhang, Q.; Yap, C. C. R.; Tay, B. K.; Edwin, T. H. T.; Olivier, A.; Baillargeat, D. From Bulk to Monolayer MoS_2: Evolution of Raman Scattering. *Adv. Funct. Mater.* **2012**, *22*, 1385−1390.
(35) Pimenta, M. A.; del Corro, E.; Carvalho, B. R.; Fantini, C.; Malard, L. M. Comparative Study of Raman Spectroscopy in Graphene and MoS_2-Type Transition Metal Dichalcogenides. *Acc. Chem. Res.* **2015**, *48*, 41−47.
(36) Li, M.; Selvarajan, P.; Wang, S.; Wan, T.; Xi, S.; Wang, X.; Xue, J.; Indirathankam, S. C.; Geng, X.; Qiao, L.; Vinu, A.; Chu, D.; Yi, J. Thermostable 1T-MoS_2 Nanosheets Achieved by Spontaneous Intercalation of Cu Single Atoms at Room Temperature and Their Enhanced HER Performance. *Small Struct.* **2023**, *4*, 2300010.
(37) Li, M.; Cai, B.; Tian, R.; Yu, X.; Breese, M. B. H.; Chu, X.; Han, Z.; Li, S.; Joshi, R.; Vinu, A.; Wan, T.; Ao, Z.; Yi, J.; Chu, D. Vanadium doped 1T MoS_2 nanosheets for highly efficient electrocatalytic hydrogen evolution in both acidic and alkaline solutions. *Chem. Eng. J.* **2021**, *409*, 128158.
(38) Wu, Z. Z.; Tang, C. Y.; Zhou, P.; Liu, Z. H.; Xu, Y. S.; Wang, D. Z.; Fang, B. Z. Enhanced Hydrogen Evolution Catalysis from Osmotically Swollen Ammoniated MoS_2. *J. Mater. Chem. A* **2015**, *3*, 13050−13056.
(39) Li, J.; Wang, D.; Ma, H.; Li, M.; Pan, Z.; Jiang, Y.; Tian, Z. Ionic Liquid Assisted Hydrothermal Synthesis of MoS_2 Double-Shell Polyhedral Cages with Enhanced Catalytic Hydrogenation Activities. *RSC Adv.* **2017**, *7*, 23523−23529.
(40) Li, M.; Wang, D.; Li, J.; Pan, Z.; Ma, H.; Jiang, Y.; Tian, Z.; Lu, A. Surfactant-Assisted Hydrothermally Synthesized MoS_2 Samples with Controllable Morphologies and Structures for Anthracene Hydrogenation. *Chin. J. Catal.* **2017**, *38*, 597−606.
(41) Jiang, Y.; Wang, D.; Pan, Z.; Ma, H.; Li, M.; Li, J.; Zheng, A.; Lv, G.; Tian, Z. Microemulsion-Mediated Hydrothermal Synthesis of Flower-Like MoS_2 Nanomaterials with Enhanced Catalytic Activities for Anthracene Hydrogenation. *Front. Chem. Sci. Eng.* **2018**, *12*, 32−42.
(42) Wang, D.; Li, J.; Ma, H.; Yang, C.; Pan, Z.; Qu, W.; Tian, Z. Layer-Structure Adjustable MoS_2 Catalysts for the Slurry-Phase Hydrogenation of Polycyclic Aromatic Hydrocarbons. *J. Energy Chem.* **2021**, *63*, 294−304.
(43) Liang, K. S.; Chianelli, R. R.; Chien, F. Z.; Moss, S. C. Structure of Poorly Crystalline MoS_2 - A Modeling Study. *J. Non-Cryst. Solids* **1986**, *79*, 251−273.
(44) De la Rosa, M. P.; Texier, S.; Berhault, G.; Camacho, A.; Yacaman, M. J.; Mehta, A.; Fuentes, S.; Montoya, J. A.; Murrieta, F.; Chianelli, R. R. Structural Studies of Catalytically Stabilized Model and Industrial-Supported Hydrodesulfurization Catalysts. *J. Catal.* **2004**, *225*, 288−299.
(45) Berhault, G.; Perez De la Rosa, M.; Mehta, A.; Yacaman, M. J.; Chianelli, R. R. The Single-Layered Morphology of Supported MoS_2-Based Catalysts - the Role of the Cobalt Promoter and Its Effects in the Hydrodesulfurization of Dibenzothiophene. *Appl. Catal., A* **2008**, *345*, 80−88.
(46) Li, Y.; Li, A.; Li, F.; Liu, D.; Chai, Y.; Liu, C. Application of HF Etching in a HRTEM Study of Supported MoS_2 Catalysts. *J. Catal.* **2014**, *317*, 240−252.
(47) Yang, C.; Wang, D.; Huang, R.; Han, J.; Ta, N.; Ma, H.; Qu, W.; Pan, Z.; Wang, C.; Tian, Z. Highly Active and Stable MoS_2-TiO_2 Nanocomposite Catalyst for Slurry-Phase Phenanthrene Hydrogenation. *Chin. J. Catal.* **2023**, *46*, 125−136.
(48) Kasztelan, S.; Toulhoat, H.; Grimblot, J.; Bonnelle, J. P. A Geometrical Model of the Active Phase of Hydrotreating Catalysts. *Appl. Catal.* **1984**, *13*, 127−159.
(49) Kim, K. D.; Lee, Y. K. Active Phase of Dispersed MoS_2 Catalysts for Slurry Phase Hydrocracking of Vacuum Residue. *J. Catal.* **2019**, *369*, 111−121.
(50) Daage, M.; Chianelli, R. R. Structure-Function Relations in Molybdenum Sulfide Catalysts: The "Rim-Edge" Model. *J. Catal.* **1994**, *149*, 414−427.
(51) Huang, R.; Yang, C.; Ta, N.; Ma, H.; Qu, W.; Wang, C.; Pan, Z.; Wang, D.; Tian, Z. Constructing Layer-by-Layer Self-Assembly MoS_2/C Nanomaterials by a One-Step Hydrothermal Method for Catalytic Hydrogenation of Phenanthrene. *Chem. Commun.* **2023**, *59*, 10765−10768.
(52) Liu, P.; Zhao, Y.; Qin, R.; Mo, S.; Chen, G.; Gu, L.; Chevrier, D.; Zhang, P.; Guo, Q.; Zang, D.; Wu, B.; Fu, G.; Zheng, N. Photochemical Route for Synthesizing Atomically Dispersed Palladium Catalysts. *Science* **2016**, *352*, 797−800.
(53) Li, J.; Liu, H. X.; Gou, W.; Zhang, M.; Xia, Z.; Zhang, S.; Chang, C. R.; Ma, Y.; Qu, Y. Ethylene-Glycol Ligand Environment Facilitates Highly Efficient Hydrogen Evolution of Pt/CoP through Proton Concentration and Hydrogen Spillover. *Energy Environ. Sci.* **2019**, *12*, 2298−2304.

https://doi.org/10.1021/acsomega.4c01846
ACS Omega 2024, 9, 23843−23852